Spatial/Spectral Analysis of Hyperspectral Image Data

Antonio Plaza, Pablo Martínez, Javier Plaza and Rosa Pérez
Neural Networks and Signal Processing Group (GRNPS)
Computer Science Department, University of Extremadura
Avda. de la Universidad s/n, 10071 Cáceres, Spain
E-mail: aplaza@unex.es

Abstract— **The integration of spatial and spectral responses in hyperspectral image data analysis has been identified as a desirable objective by the remote sensing community. However, most available attempts are based on the consideration of spectral information separately from spatial information, and thus the two types of information are not treated simultaneously. In this paper, we describe our background in applying joint spatial/spectral techniques for full (pure)- and mixed-pixel classification of hyperspectral image data. Most of the techniques described in this work are based on classic mathematical morphology theory, which provides a remarkable framework to achieve the desired integration. The performance of the proposed methodologies is demonstrated by comparing them to other well-known pure- and mixed-pixel classifiers, using both simulated and real hyperspectral data collected by the NASA/JPL-AVIRIS and DLR-DAIS 7915 imaging spectrometers.**

Keywords-hyperspectral analysis; spatial/spectral integration; mathematical morphology; endmember extraction; morphological profiles.

I. INTRODUCTION

Recent advances in sensor technology have led to the development of hyperspectral instruments, capable of collecting hundreds of images corresponding to different wavelength channels, for the same area on the surface of the Earth [1]. A diverse array of analysis techniques has been applied to hyperspectral image data during the last decade [2]-[4]. They are inherently either full (pure)-pixel techniques or mixed-pixel techniques, where each pixel vector in a hyperspectral image records the spectral information. The underlying assumption governing full-pixel techniques is that each pixel vector measures the response of one predominantly underlying material at each site in a scene. In contrast, the underlying assumption governing mixed-pixel techniques is that each pixel vector measures the response of multiple underlying materials at each site. An image is often a combination of the two situations, where a few sites in a scene can be regarded as pure materials, but many others are mixtures of materials.

Full-pixel techniques include the method of spectral matching, along with various supervised and unsupervised scene segmentation approaches, based on statistical and pattern recognition-based schemes [4]. Techniques include statistical linear discrimination, quadratic multivariate classifiers, and neural networks [2]. On other hand, mixed-pixel techniques have overcome some of the weaknesses of full-pixel approaches by using linear statistical modeling and signal processing-based schemes [3]. They are inherently either nonlinear or linear approaches which rely on spectral mixture modelling. Although sub-pixel nonlinear mixing can be important for some types of analysis, the effects of multiple scattering in the majority of applications are assumed to be negligible if a linear model is used [5]. In such cases, the rich spectral information contained in the hyperspectral data cube is used to model mixed pixels in terms of linear combinations of spectrally pure samples (usually called endmembers in hyperspectral analysis terminology).

Despite the inherent spatial-spectral duality that resides in hyperspectral data cubes, most available processing techniques tend to focus exclusively on the spectral domain. As a result, data analysis is carried out without incorporating information on the spatially adjacent data; i.e. the data is treated not as an image but as an unordered listing of spectral measurements where the spatial coordinates can be shuffled arbitrarily without affecting analysis [6]. However, one of the distinguishing properties of hyperspectral data, as collected by available imaging spectrometers, is the multivariate information coupled with a two-dimensional (2-D) pictorial representation amenable to image interpretation [7]. Subsequently, although image processing in engineering literature is not directed to the analysis of hyperspectral data, there is a need to incorporate the image representation of the data in the analysis. By taking into account the complementary nature of spatial and spectral information in simultaneous fashion, it is possible to alleviate the problems related to each of them taken separately [6]. In addition, the incorporation of spatial/spectral models may improve existing full- and mixed-pixel classification methods.

In this research, we consider hyperspectral image analysis from a broader perspective than the individual methods listed above. Instead of focusing exclusively on the spectral information contained in the data, we focus on the analysis of spatial and spectral patterns simultaneously. In previous work [8], [9], we have explored the application of mathematical morphology operations to integrate both spatial and spectral responses in hyperspectral data analysis. Classic mathematical morphology [10], [11] is a non-linear spatial processing technique that provides a remarkable framework to achieve the desired integration. Morphology was originally defined for binary images and has been extended to the greyscale [12] and color [13] image cases, but it has been seldom used to process

This research has been supported in part by the European Community under HPRI-1999-00057 project.

multi/hyperspectral imagery. In contrast, greyscale morphology has been widely used in the fields of geoscience and remote sensing [14]. In this work, we provide detailed insight on the use of extended morphological operations for full- and mixed-pixel characterization in hyperspectral data. The former goal is achieved by the calculation of extended scale-space and scale-orientation morphological profiles [15] at each image pixel, thus alllowing to create a feature set which is very efficient in discrimination of different image features. The latter objective is obtained by a novel application of extended morphological operations to automated extraction of endmembers from hyperspectral data by combining spatial and spectral information. Our research is structured as follows: Section II describes the approach followed for extension of classic morphological operations to hyperspectral imagery. Section III illustrates the proposed morphological endmember extraction method. In Section IV, a framework for the calculation of morphological profiles for hyperspectral data analysis is described, and a number of examples are provided. Sections V and VI respectively contain an evaluation of the proposed mixed-pixel and full-pixel classification approaches, along with a comparison to other existing approaches using both simulated and real data. Finally, section VII includes some concluding statements and comments on plausible future research.

II. Extended Mathematical Morphology

The two basic operations of classic mathematical morphology are erosion and dilation [10]. Following a usual notation [16], let us consider a grayscale image f, defined on a space E. Typically, E is the 2-D continuous space R^2 or the 2-D discrete space Z^2. In the following, we refer to morphological operations defined on the discrete space. The flat erosion of f by $B \subset Z^2$, where B is called a 'structuring element' (SE), is defined by the following expression

$$(f \otimes B)(x,y) = \bigwedge_{(s,t)\in Z^2(B)} f(x+s, y+t), (x,y) \in Z^2, \quad (1)$$

where $Z^2(B)$ denotes the set of discrete spatial coordinates associated to pixels lying within the neighborhood defined by B and $\bigwedge$ denotes the minimum. On the other hand, the flat dilation of f by B is defined by

$$(f \oplus B)(x,y) = \bigvee_{(s,t)\in Z^2(B)} f(x-s, y-t), (x,y) \in Z^2, \quad (2)$$

where $\bigvee$ denotes the maximum. Using the same notation above, the composition

$$(f \circ B)(x,y) = [(f \otimes B) \oplus B](x,y), (x,y) \in Z^2, \quad (3)$$

yields a flat opening, an operator that is increasing, anti-extensive, and idempotent [11]. On the other hand, the composition

$$(f \bullet B)(x,y) = [(f \oplus B) \otimes B](x,y), (x,y) \in Z^2. \quad (4)$$

is called a flat closing, an operator that is increasing, extensive, and idempotent. A morphological operator is called a morphological filter if it is increasing and idempotent [11]. It is a common practice to use opening and closing morphological filters in order to isolate bright (opening) and dark (closing) structures in grayscale images, where bright/dark means brighter/darker than the surrounding structures in the image.

In order to illustrate the two basic morphological operations, i.e. erosion and dilation, let B be a flat 3x3 pixel SE. An erosion operation using B has been applied to a high spatial resolution (1.2 meters per pixel) grayscale image obtained from a portion of the spectral band collected at 0.584 μm wavelength by the DLR-ROSIS imaging spectrometer over a "Dehesa" ecosystem (mainly formed by cork-oak trees, soil and pasture) in Caceres, SW Spain. In Fig. 1(a), cork-oak trees appear as dark spots, pasture areas are represented by gray tones, and soil zones are associated with bright pixels. As Fig. 1(b) points out, the application of a mono-channel flat erosion operation using B to the original scene is a new image (with the same dimensions as the original) where darker zones are developed regarding the size and shape of the SE. In contrast, a flat dilation has the global effect of shrinking the darker zones and enlarging the bright areas of the image [see Fig. 1(c)].

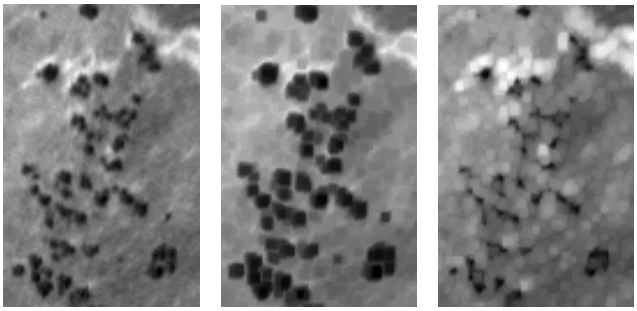

a) b) c)

Figure 1. (a) Band at 0.584 μm of original ROSIS hyperspectral image. (b) Resulting image after applying a grayscale erosion to (a) using a flat 3x3 structuring element. (c) Resulting image after applying a grayscale dilation to (a) using a flat 3x3 structuring element.

In order to extend basic morphological operations to hyperspectral images, let us now consider an image $\boldsymbol{f}$, defined on the (N-D) continuous morphological space, where N is the number of spectral channels. An ordering relation can be imposed in the set of pixels lying within a flat SE, denoted by B, by defining metrics that calculate the cumulative distance between one particular pixel $\boldsymbol{f}(x,y)$, where $\boldsymbol{f}(x,y)$ denotes an N-D vector at discrete spatial coordinates $(x,y) \in Z^2$, and every other pixel in the neighborhood given by B. Based on the previous considerations, flat extended dilation and flat extended erosion can be respectively defined as follows

$$(\boldsymbol{f} \oplus B)(x,y) = \arg\left\{ \bigwedge_{(s,t)\in Z^2(B)} \left[\sum_s \sum_t \mathrm{Dist}(\boldsymbol{f}(x,y), \boldsymbol{f}(x+s, y+t)) \right] \right\} \quad (5)$$

$$(\boldsymbol{f} \otimes B)(x, y) = \arg\left\{ \bigvee_{(s,t)\in Z^2(B)} \left[\sum_s \sum_t \mathrm{Dist}\big(\boldsymbol{f}(x, y), \boldsymbol{f}(x-s, y-t)\big) \right] \right\} \quad (6)$$

where Dist is a point-wise distance measure between two $N-D$ vectors. The choice of Dist is a key topic in the resulting ordering relation. This study has been presented in previous work [8], [9]. In this paper, Dist refers to the spectral angle (SAD) distance, one of the standard metrics in hyperspectral analysis. Our choice of SAD is mainly based on the fact that this distance is invariant to multiplicative scaling that may arise due to different illumination conditions and sensor observation angle [5]. It should be noted that the arg operator in (5) and (6) selects the $N-D$ pixel vector that respectively maximizes and minimizes the cumulative distance value between $\boldsymbol{f}(x, y)$ and its neighboring pixels according to B. Hence, the use of SAD as the standard distance metric allows us to impose a partial order relationship of the vectors within an SE in terms of their spectral purity. It is important to notice that, regardless of the distance measure used, the proposed operators are vector preserving, i.e. no vector (constituent) that is not present in the input data is generated as a result of the extension process [9].

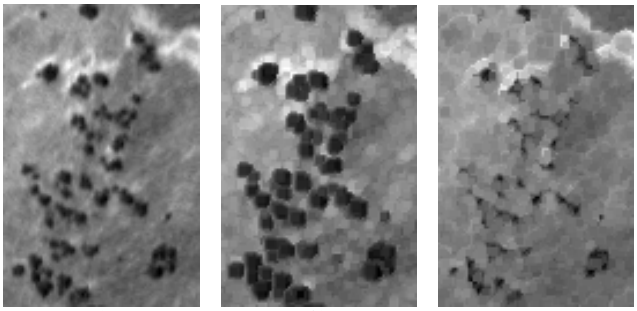

a) b) c)

Figure 2. (a) Band at 0.584 μm of original ROSIS hyperspectral image. (b) Band at 0.584 μm of the hyperspectral image obtained after applying an extended erosion to the original image using a flat 3x3 structuring element. (c) Band at 0.584 μm of the hyperspectral image obtained after applying an extended dilation to the original image using a flat 3x3 structuring element.

For illustrative purposes, let B be a flat 3x3 SE. If this element is moved, pixel by pixel, through the ROSIS imaging spectrometer data set introduced above, then the SE defines a local spatial search area around each pixel. The result of applying an extended erosion/dilation operation to a hyperspectral dataset using B is a new data cube, with exactly the same dimensions as the original, where each pixel has been replaced by the maximum/minimum of the neighborhood defined by the flat SE. As can be examined in Fig. 2, extended dilation [see Fig. 2(b)] has the effect of expanding zones with "pure" spectral signatures (in the example, cork-oak and soil areas are developed). Most of the pasture areas in the ROSIS scene are made up of soil mixtures and pasture because of the early growth stage of pasture at the time of sensor data acquisition (July 2001). This effect can be noticed in Fig. 2(c), where the erosion operation expands gray-tone ("mixed") areas and shrinks both dark (cork-oak) and bright (pure soil) areas. With the two previous operations, the construction of extended flat opening and closing operations is straightforward.

III. Endmember Extraction for Mixed-Pixel Analysis Using Extended Morphological Operations

Before describing existing approaches for endmember extraction in hyperspectral imagery and introducing our proposed approach, we list key advantages in the use of extended morphological operations to perform the above task [8]. A first major point is that endmember selection is basically a nonlinear procedure, much like morphological operations. Furthermore, mathematical morphology allows for the introduction of a local-to-global approach in the search for endmembers by using spatial kernels (structuring elements in the morphology jargon). These items define local neighborhoods around each pixel that can be applied to search local convexities within the data cloud, and to use the spatial correlation between the data. Endmembers can be identified by following an iterative process where pixels in close proximity in the spatial domain compete against each other in terms of their convexity or spectral purity. As a result, a local representative in a neighborhood is selected and compared to other locally selected pixels. The adoption of this approach leads to the incorporation of spatial information into the endmember determination procedure. As a final major point, morphological operations are implemented by replacing a pixel with a neighbor that satisfies a certain condition. Since an endmember is defined as a spectrally pure pixel that describes several mixed pixels in the scene, extended morphological operations can obviously contribute to locating suitable pixels that replace others in the scene according to some desired particularity of the pixel, for example, its spectral purity.

A. Background on endmember extraction techniques

A number of fully- and semi-automated algorithms have been proposed over the past decade to accomplish the complex task of finding appropriate endmembers for spectral unmixing in multi/hyperspectral data. Next, we provide an overview of some of the most successful approaches.

1) Pixel Purity Index (PPI). This semi-automated method proceeds by generating a large number of random $N-D$ vectors, also called "skewers" [17], through the dataset. Every data point is projected onto each skewer, and the data points which correspond to extrema in the direction of a skewer are identified and placed on a list. The pixels with the highest tallies are considered the purest ones, and a pixel count provides a "pixel purity index". An $N-D$ visualization procedure is then applied to select a final list of endmembers.

2) N-FINDR. This fully automated approach finds the set of pixels with the largest possible volume by "inflating" a simplex within the data [18]. A random set of vectors is initially selected. In order to refine the initial estimate of endmembers, every pixel in the image must be evaluated in terms of pixel purity likelihood or nearly pure statehood. To achieve this, a trial volume is calculated for every pixel in each endmember position by replacing that endmember and finding the volume. If the replacement results in a volume increase, the pixel replaces the endmember. This procedure is repeated until there are no more replacements of end-members.

3) Optical Real-time Adaptative Spectral Identification System (ORASIS). This fully automated approach, developed at Naval Research Laboratory, uses a process called Exemplar Selection to trim the data set [19]. This procedure rejects redundant spectra by calculating the angle between spectral vectors. The procedure then finds a basis set of much lower dimension than the original data by a modified Gram-Schmidt process. The exemplar spectra are then projected onto this basis sub-space and a simplex is found through a minimum volume transform.

4) Iterative Error Analysis (IEA). In the fully automated IEA algorithm, an initial vector, usually the mean spectrum of the data, is selected to start the process. A constrained unmixing is then performed and an error image is formed. The average score of vectors with higher error (distance from the initial vector) is assumed to be the first endmember. Another constrained unmixing is then performed and the error image is formed. The average score of vectors with greater errors (distance from the first endmember) is assumed to be the second endmember. This process is continued until a predetermined number of endmembers is found [20].

5) Convex Cone Analysis (CCA). This fully automated approach is based on the fact that vectors formed by discrete radiance/reflectance spectra can be expressed as linear combinations of nonnegative components, which lie inside a nonnegative, convex region [21]. The objective of CCA is to find the boundary points for this region. To implement this concept, the method finds the eigenvectors of the sample spectral correlation matrix of the image, and selects those eigenvectors corresponding to the E largest eigenvalues (where E is the a priori number of endmembers to model). The method then looks for the boundaries of the convex cone, where the linear combinations of these eigenvectors produce vectors that are strictly nonnegative.

B. Automated morphological endmember extraction (AMEE)

Contrary to the methods described in section A, which rely on spectral properties of the data alone, we propose to use a morphological approach where spatial and spectral information are equally employed to derive endmembers [8]. A general block diagram of the proposed method is shown in Fig. 3. As shown in Fig. 3, the input to the method is the full data cube, with no previous dimensionality reduction or pre-processing. Parameter L refers to the number of iterations that the algorithm performs. Parameters S_{min} and S_{max} respectively denote the minimum and maximum SE sizes that will be considered in the process. The minimum SE size S_{min} is first considered. The SE is moved through all the pixels of the image, and the spectrally purest pixel and the spectrally most highly mixed pixel be obtained at each SE neighborhood by extended morphological dilation and erosion operations. A morphological eccentricity index (MEI) value is associated to the purest pixel by comparing the result of the dilation to the result of erosion. The previously described operation is repeated by using SE's of progressively increased size, and the algorithm performs as many iterations as needed until the maximum SE size S_{max} is achieved. The associated MEI value of selected pixels at subsequent iterations is updated by means of newly obtained values, as a larger spatial context is considered, and a final MEI image is generated after L iterations. This approach ensures a complete spatial/spectral description of the image and provides an efficient tool to integrate both types of information simultaneously.

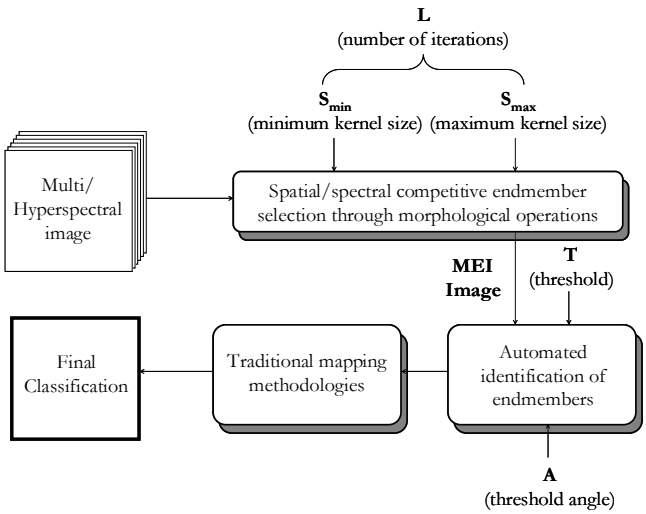

Figure 3. Block diagram of Automated Morphological Endmember Extraction (AMEE) method.

Automated endmember selection is then performed from the MEI image obtained in the competitive endmember selection step by an automated threshold value T [8]. The final selection is refined by a region-growing procedure that incorporates neighboring pixels that are sufficiently similar (according to a certain threshold angle parameter A) to the regions obtained after thresholding [22]. Mean spectra are obtained for the resulting regions after the region-growing process, and a final set of endmembers is generated. Traditional spectral mixture-based methodologies such as linear spectral unmixing (LSU) [5] or fully-constrained linear spectral unmixing (FCLSU) [23] can now be used for endmember fractional abundance estimation at a sub-pixel level.

IV. Extended Morphological Profiles for Full-Pixel Characterization

Contrary to the methods presented in the previous section, which are based on the concept of mixed-pixel analysis, our main goal in this section is to incorporate the idea of multi-scale analysis by extended morphological operations into full-pixel classification of hyperspectral data. As shown before, morphological filters are characterized by the size and shape of the considered SE. However, if the searched patterns do not have regular properties across the scene, an adaptative scheme is needed to ensure that the correct SE is considered at each pixel. This need consequently poses the problem of adequate parameter selection. As reported in previous work by Pesaresi & Benediktsson [15], parameter selection can be achieved by plotting morphological opening-/closing-by-reconstruction operation output at each pixel against the value of a varying parameter. The resulting plot is called a morphological profile [15], where the varying parameter is usually the size of the SE.

Morphological profiles present optimal properties for full-pixel classification of hyperspectral image data, as reported in previous work [24]. These profiles can also be constructed for a parameter related to the orientation of line segment structuring elements [25]. Simple derivative rules can be applied to morphological profiles in order to determine the most appropriate parameter value for each pixel. In this section, we detail the process followed to extend the concepts of morphological profiles and derivative analysis to hyperspectral data by addressing two different types of extended profiles, i.e. those where the varying parameter is the size of the SE (scale-space profiles) and those where both the SE size and orientation are considered (scale-orientation profiles).

A. Scale-space morphological profiles

Morphological profiles in grayscale imagery are based on opening- and closing-by-reconstruction, a special class of morphological filters that have proven to be very successful for multi-scale image processing [10]. These filters do not introduce discontinuities, and therefore preserve the shapes observed in input images. The basic contrast imposed by conventional opening and closing versus reconstruction-based opening and closing, can be described as follows: conventional opening and closing remove the parts of the objects that do not fit in the SE, whereas opening and closing by reconstruction either completely removes the features or retains them as a whole. In order to extend reconstruction-based opening and closing operations to hyperspectral imagery, let us consider a hyperspectral image $\boldsymbol{f}$ defined on R^N. Given an SE (designed by B) of minimal size, extended opening by reconstruction is defined by

$$(\boldsymbol{f} \circ B)^{k}(x,y) = \bigvee_{k \geq 1} \left[\delta_B^{k}(\boldsymbol{f} \circ B \mid \boldsymbol{f})\right](x,y) \tag{7}$$

where

$$\left[\delta_B^{k}(\boldsymbol{f} \circ B \mid \boldsymbol{f})\right](x,y) = \left[\overbrace{\delta_B \delta_B \cdots \delta_B}^{\text{k times}}(\boldsymbol{f} \circ B \mid \boldsymbol{f})\right](x,y). \tag{8}$$

The elementary term $\left[\delta_B(\boldsymbol{f} \circ B \mid \boldsymbol{f})\right](x,y)$ is an extended geodesic dilation [10], defined as the maximum of the elementary dilation of $\boldsymbol{f} \circ B$ using B at pixel (x,y) and the value of $\boldsymbol{f}(x,y)$,

$$\left[\delta_B(\boldsymbol{f} \circ B \mid \boldsymbol{f})\right](x,y) = \left\{\left[(\boldsymbol{f} \circ B) \oplus B\right](x,y)\right\} \bigvee \left\{\boldsymbol{f}(x,y)\right\}. \tag{9}$$

As shown in (8), this operation is repeated *k* times until idempotence is reached. In a similar fashion, extended morphological closing by reconstruction is given by the following expression

$$(\boldsymbol{f} \bullet B)^{k}(x,y) = \bigwedge_{k \geq 1} \left[\varepsilon_B^{k}(\boldsymbol{f} \bullet B \mid \boldsymbol{f})\right](x,y), \tag{10}$$

where

$$\left[\varepsilon_B^{k}(\boldsymbol{f} \bullet B \mid \boldsymbol{f})\right](x,y) = \left[\overbrace{\varepsilon_B \varepsilon_B \cdots \varepsilon_B}^{\text{k times}}(\boldsymbol{f} \bullet B \mid \boldsymbol{f})\right](x,y). \tag{11}$$

The elementary term $\left[\varepsilon_B(\boldsymbol{f} \bullet B \mid \boldsymbol{f})\right](x,y)$ is an extended geodesic erosion [10], defined as the minimum of the elementary erosion of $\boldsymbol{f} \bullet B$ using B at pixel (x,y) and the value of $\boldsymbol{f}(x,y)$,

$$\left[\varepsilon_B(\boldsymbol{f} \bullet B \mid \boldsymbol{f})\right](x,y) = \left\{\left[(\boldsymbol{f} \bullet B) \otimes B\right](x,y)\right\} \bigwedge \left\{\boldsymbol{f}(x,y)\right\}. \tag{12}$$

Using (7) and (10), scale-space morphological profiles are simply defined as follows [26]. Let the vector $\boldsymbol{p}_k^{\circ}(x,y)$ be the extended opening by reconstruction profile at the point (x,y) of the image $\boldsymbol{f}$, defined by:

$$\boldsymbol{p}_k^{\circ}(x,y) = \left\{(\boldsymbol{f} \circ B)^{\lambda}(x,y)\right\}, \quad \lambda = \{0, \ldots, k\}, \tag{13}$$

And let $\boldsymbol{p}_k^{\bullet}(x,y)$ be the extended closing by reconstruction profile at the point (x,y) of the image $\boldsymbol{f}$, defined by:

$$\boldsymbol{p}_k^{\bullet}(x,y) = \left\{(\boldsymbol{f} \bullet B)^{\lambda}(x,y)\right\}, \quad \lambda = \{0, \ldots, k\}. \tag{14}$$

Here $(\boldsymbol{f} \bullet B)^{0}(x,y) = \boldsymbol{f}(x,y) = (\boldsymbol{f} \circ B)^{0}(x,y)$ for $\lambda = 0$ by the definition of extended opening- and closing-by-reconstruction [10]. We define the derivative of the extended opening profile $\Delta\boldsymbol{p}_k^{\circ}(x,y)$ as the vector

$$\Delta\boldsymbol{p}_k^{\circ}(x,y) = \left\{\mathrm{Dist}\left[(\boldsymbol{f} \circ B)^{\lambda}(x,y), (\boldsymbol{f} \circ B)^{\lambda-1}(x,y)\right]\right\}, \lambda = \{1, \ldots, k\}. \tag{15}$$

By duality, the derivative of the closing profile $\Delta\boldsymbol{p}_k^{\bullet}(x,y)$ is the vector

$$\Delta\boldsymbol{p}_k^{\bullet}(x,y) = \left\{\mathrm{Dist}\left[(\boldsymbol{f} \bullet B)^{\lambda}(x,y), (\boldsymbol{f} \bullet B)^{\lambda-1}(x,y)\right]\right\}, \lambda = \{1, \ldots, k\}. \tag{16}$$

where Dist is a point-wise distance measure. As mentioned before, in this work Dist refers to the spectral angle distance (SAD), selected because it is invariant to unknown multiplicative scalings that may arise due to atmospheric transmission and angular observation effects in the data.

In Fig. 4, the procedure followed in this section to obtain extended morphological profiles is illustrated by using four target objects in a ROSIS hyperspectral image: a small cork-oak tree [see Fig. 4(a)], a pure soil area [Fig. 4(b)], a medium-sized cork-oak tree [Fig. 4(c)], and a mixed area formed by soil and pasture, surrounded by pure soil [Fig. 4(d)]. Extended morphological profiles were constructed for the above pixels.

The resulting opening and closing profiles were combined in $3-D$ plots, where the spectral signature of the analyzed pixel $\boldsymbol{f}(x,y)$, denoted by P in the plots, is shown along with the resulting spectral signatures obtained after applying a series of opening- and-closing-by-reconstruction operations using different SE sizes. A range of SE's was considered in experiments, based on three iterations of the elementary eight-connected 3x3 SE [using (8) and (11), respectively]. These iterations were labeled in the plots as $Ok=(\boldsymbol{f}\circ B)^k(x,y)$ for the opening series, and $Ck=(\boldsymbol{f}\bullet B)^k(x,y)$ for the closing series, where $k=\{1,2,3\}$. As can be observed in Figs. 4(a-c), pure pixels remain indifferent to the three closing-by-reconstruction iterations, but are replaced during the opening-by-reconstruction process. Similarly, it is shown in Fig. 4(d) that the mixed pixel remains indifferent to the three opening-by-reconstruction iterations, but is replaced in the closing series. The step of the opening/closing series iteration at which the pixel is replaced provides an intuitive idea of both the spectral purity of the pixel and the spatial distribution of the object in the scene.

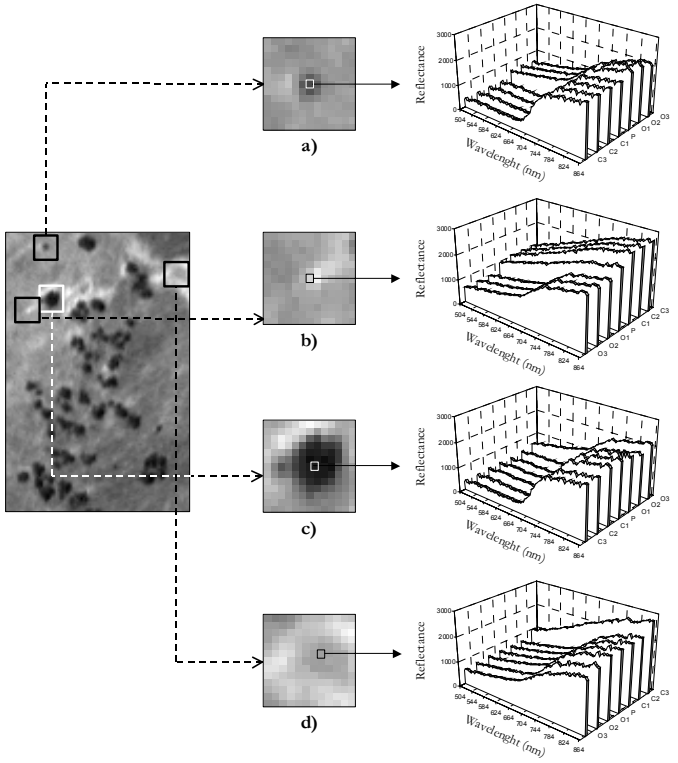

Figure 4. Extended morphological profiles associated to pixels belonging to four target objects in a ROSIS hyperspectral scene: (a) Small cork-oak tree, (b) Pure soil area, (c) Medium-sized cork-oak tree, (d) Mixed area formed by soil and pasture, surrounded by pure soil.

Fig. 5 shows graphs where the resulting opening and closing derivative profiles for each analyzed pixel in Fig. 4 are combined in single $2-D$ plots. These plots can be interpreted as histograms that show the level of the derivative relative to the opening and closing series for each step of the iteration [15]. As a result, pixels that are spectrally purer than their adjacent components have a combined derivative profile that is unbalanced to the right (opening series), as shown in Figs. 5(a), 5(b) and 5(c). In contrast, mixed pixels show a derivative profile that is unbalanced to the left (closing series), as illustrated in Fig. 5(d). These profiles provide an indication of the morphological characteristic of a certain spectral feature in the given spatial domain range, which can be used to characterize each hyperspectral image pixel using a joint spatial/spectral criterion.

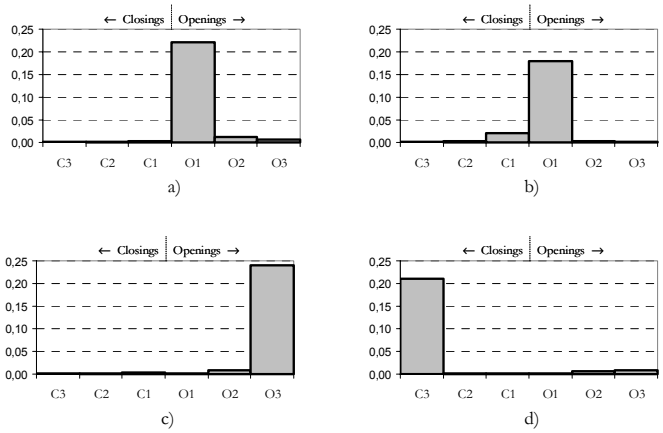

Figure 5. Derivatives of the morphological profiles associated with target pixels in Fig. 4: (a) Small cork-oak tree, (b) Pure soil area, (c) Medium-sized cork-oak tree, (d) Mixed area formed by soil and pasture, surrounded by pure soil.

B. Scale-orientation morphological profiles

Directional morphological profiles have been created for greyscale imagery by performing morphological opening- and closing-by-reconstruction with line segment SE's of varying orientation [25]. The resulting filter output is plotted against the orientation of the line segment. If all orientations output the same value, it means that there is no orientation for the chosen SE size. If required by the application under study, rather than selecting a unique SE size, scale and orientation information at each pixel can be extracted by plotting the morphological filter output against the orientation of line segment SE's of progressively increased size. The resulting plot is called a scale-orientation morphological profile [27]. In order to extend the idea of scale-orientation profiles to hyperspectral imagery, we define the directional morphological profile at the point (x,y) of a hyperspectral image $\boldsymbol{f}$ as follows. Given a line segment SE of minimal size B_θ, where θ refers to the orientation angle of the line segment in radians, we define the extended scale-orientation opening-by-reconstruction morphological profile $\boldsymbol{dp}_k^\circ(x,y)$ as

$$\boldsymbol{dp}_k^\circ(x,y)=\left\{(\boldsymbol{f}\circ B_\theta)^\lambda(x,y)\right\},\ \lambda=\{0,\ldots,k\},\ \theta=\{0,\ldots,2\pi\}\text{radians}\quad(17)$$

Similarly, we define the extended scale-orientation closing-by-reconstruction morphological profile $\boldsymbol{dp}_k^\bullet(x,y)$ by the following expression

$$\boldsymbol{dp}_k^\bullet(x,y)=\left\{(\boldsymbol{f}\bullet B_\theta)^\lambda(x,y)\right\},\ \lambda=\{0,\ldots,k\},\ \theta=\{0,\ldots,2\pi\}\text{radians}\quad(18)$$

Regardless of the considered orientation angle, $(\boldsymbol{f} \bullet B_\theta)^0(x,y) = \boldsymbol{f}(x,y) = (\boldsymbol{f} \circ B_\theta)^0(x,y)$ for $\lambda = 0$ by the definition of extended opening- and closing-by-reconstruction [10]. With the above result in mind, we can define the derivative of the scale-orientation opening profile $\Delta \boldsymbol{dp}^{\circ}_{k}(x,y)$ as the matrix

$$\Delta \boldsymbol{dp}^{\circ}_{k}(x,y) = \left\{ \mathrm{Dist}\left[(\boldsymbol{f} \circ B_\theta)^{\lambda}(x,y), (\boldsymbol{f} \circ B_\theta)^{\lambda-1}(x,y) \right] \right\}, \lambda = \{1, \ldots, k\}, \quad \theta = \{0, \ldots, 2\pi\} \text{ radians} \tag{19}$$

By duality, the derivative of the scale-orientation closing profile $\Delta \boldsymbol{dp}^{\bullet}_{k}(x,y)$ is defined as the matrix

$$\Delta \boldsymbol{dp}^{\bullet}_{k}(x,y) = \left\{ \mathrm{Dist}\left[(\boldsymbol{f} \bullet B_\theta)^{\lambda}(x,y), (\boldsymbol{f} \bullet B_\theta)^{\lambda-1}(x,y) \right] \right\}, \lambda = \{1, \ldots, k\}, \quad \theta = \{0, \ldots, 2\pi\} \text{ radians} \tag{20}$$

If we consider Dist as the spectral angle distance (SAD), we can define the orientation at a given hyperspectral image pixel $\boldsymbol{f}(x,y)$ as the orientation of the line segment SE that maximizes the SAD between the spectral signature in the original image at the point (x,y) and the spectral signature at the same location in the image filtered by the considered line segment. As a result, directional openings should produce a high response with image structures that occur in the direction of the considered line segment and, at the same time, are spectrally purer than their background. On the other hand, directional closings are appropriate to characterize image structures in the direction of the considered line segment, which are less spectrally pure (i.e. more "spectrally mixed") than their background. It should be noted that, for pixels belonging to wide (with respect to the length λ of the SE) objects of similar spectral properties, several distinct orientations may output the maximum SAD distance value. If the range of orientations at the maximum value is not connected, it means that there are oriented structures crossing each other. Scale-orientation morphological profiles can then be used to detect crossing lines, flat zones and complex image structures by taking into account both the spatial and spectral responses in the scene.

V. Mixed-Pixel Classification Results

We present in this section a comparative study of standard endmember extraction algorithms using both simulated and real hyperspectral data. Two AVIRIS imaging spectrometer datasets of the Jasper Ridge Biological Preserve (JRBP) in California have been selected for experiments [28]. The datasets are available in radiance and reflectance units (from now on, we will respectively refer to the data as AVJRBP_RAD and AVJRBP_REF). In a previous study of surface materials over JRBP, a suite of image endmembers was derived from the scenes above based on a hybrid approach combining ground knowledge and interactive analysis [29]. Two of these signatures, denoted as $\boldsymbol{r}_1$ (soil) and $\boldsymbol{r}_2$ (evergreen forest), are used as reference endmembers for simulated and real-data experiments.

A. Experiments with simulated data

In order to illustrate basic algorithmic properties of the proposed morphological approach for endmember selection, a simple simulated hyperspectral scene containing binary mixtures was created [30]. This scene, with a size of 100x100 pixels, is formed by one hundred regions, $R_1, \ldots, R_{100}$, of one-pixel width representing linear mixtures between $\boldsymbol{r}_1$ and $\boldsymbol{r}_2$. Abundance fractions of $\boldsymbol{r}_1$ at region R_i are assigned by $(i/100)$, while abundance fractions of $\boldsymbol{r}_2$ at R_i are assigned by $1-(i/100)$. The scene represents a subtle mixing scenario where $\boldsymbol{r}_1$ progressively infiltrates into $\boldsymbol{r}_2$ and vice-versa. Random noise was added to the scene to simulate contributions from ambient (clutter) and instrumental sources. For the simulations, we consider the SNR for each band as the ratio of the 50% signal level to the standard deviation of the noise, hence following the definition given in [21]. Thus, the simulated hyperspectral data are created, based on a fully-constrained linear mixture model, by the following expression

$$\boldsymbol{s}(x,y) = \left(\frac{\mathrm{SNR}}{2} + \boldsymbol{n}(x,y) \right) \cdot \sum_{j=1}^{R} \alpha_j(x,y) \cdot \boldsymbol{r}_j \,, \tag{21}$$

where $\boldsymbol{s}(x,y)$ denotes a vector containing the simulated discrete spectrum at the pixel with spatial coordinates (x,y) of the simulated image, $R = 2$ is the total number of reference spectral signatures used to simulate the scene, $\alpha_j(x,y)$ is the assigned fractional abundance of spectral signature $\boldsymbol{r}_j$ at the pixel, and $\boldsymbol{n}(x,y)$ is the noise factor. Five different SNR values, i.e. 30:1, 50:1, 70:1, 90:1 and 110:1, were considered in the generation of the simulated scene.

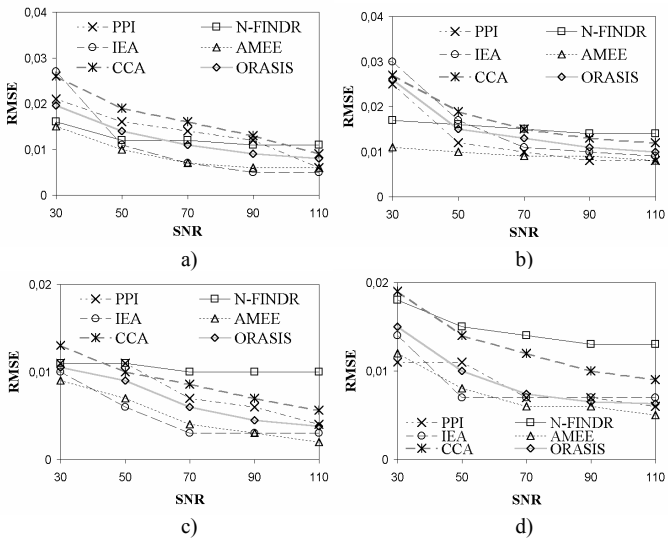

Figure 6. RMSE scores for SSMA-matched endmembers by PPI, N-FINDR, IEA, AMEE, CCA and ORASIS in CS1 at different SNR values. (a) soil endmember in radiance scene. (b) forest endmember in radiance scene. (c) soil endmember in reflectance scene. (d) forest endmember in reflectance scene.

Figs. 6(a) to 6(d) show graphs of the RMSE error scores obtained when comparing FCLSU-derived fractional abundances to ground-truth abundance fractions using the

endmembers provided by PPI, N-FINDR, ORASIS, IEA and AMEE algorithms using radiance/reflectance data and different SNR values. In general terms, the methods work slightly better with reflectance data. Overall, both AMEE and IEA produce the lowest error scores when the SNR is high or moderate. The performance of CCA and ORASIS is significantly increased when high SNR. The spatial/spectral-based method is characterized by a stable behavior with respect to SNR. This result provides some objective confirmation of our introspection: that the incorporation of spatial information reduces algorithm sensitivity to noise and outliers.

B. *Experiments with real data*

A comparative study of PPI, N-FINDR, IEA, AMEE, CCA and ORASIS in the task of extracting endmembers from real hyperspectral data is conducted in this section. Contrary to computer-simulated data, where noise and spectral mixture complexity can be easily investigated, real imagery is conditioned by additional factors, which include variations in illumination through the scene, observation angle and nonlinear mixture effects caused by multiple scattering. However, it is difficult to substantiate the individual effect of those strongly interrelated parameters on algorithm performance. In this experiment, we show a general performance comparison of algorithms on AVJRBP_RAD and AVJRBP_REF.

TABLE I. SAD-BASED SIMILARITY SCORES BETWEEN ENDMEMBERS PROVIDED BY PPI, N-FINDR, ORASIS, IEA, CCA AND AMEE AND CORRESPONDENT REFERENCE SPECTRAL SIGNATURES FOR AVJRBP_RAD AND AVJRBP_REF

	AVJRBP_RAD		**AVJRBP_REF**	
Algorithm	Soil	Forest	Soil	Forest
PPI	0.062	0.058	0.027	0.022
N-FINDR	0.077	0.064	0.028	0.025
ORASIS	0.077	0.066	0.032	0.021
IEA	0.014	0.029	0.016	0.013
CCA	0.057	0.062	0.032	0.024
AMEE	0.017	0.014	0.009	0.007

Table 1 shows SAD-based spectral similarity scores obtained by comparing the soil and evergreen forest endmembers, produced by the different methods, to reference endmembers r_1 and r_2 (a spectral similarity matching algorithm, SSMA, was used to create the associations between endmembers and reference signatures [30]). Overall, results are slightly better for reflectance data than for radiance data. The results in Table 1 reveal the importance of considering spatial and spectral information in the selection of endmembers for spectral mixture analysis. As a last final note, it is important to emphasize that the linear mixture model is not flexible enough to accommodate the full range of natural vegetation variability throughout the landscape. In order to accurately characterize the JRBP ecosystem structure, it might be necessary to account for changes in bidirectional reflectance (BRDF) in the subpixel components, since multiple scattering overestimates the results from a linear scattering model. Experiments in this section indicate that the linear mixture model, improved by the integration of spatial and spectral information in the selection of endmembers, is able to provide a good characterization of general landscape conditions.

VI. PURE-PIXEL CLASSIFICATION RESULTS

In order to illustrate full-pixel classification performance, two different experiments with real hyperspectral data sets are carried out in this section. Next, we provide a summary of the results obtained, along with a detailed discussion of the way scale-space and scale-orientation morphological profiles were used in experiments.

A. *Experiments with AVIRIS data comprising agricultural fields in Salinas Valley, California*

We have applied the proposed methods based on morphological profiles to real hyperspectral data collected by the AVIRIS imaging spectrometer in 1998 over Salinas Valley, California. The full scene consists of 512 lines by 217 samples with 224 spectral bands from 0.4 μm – 2.5 μm with a pixel resolution of 3.7mx3.7m. These data was available only as at-sensor radiance data and includes vegetables, bare soils and vineyard fields. Fig. 7 shows the entire scene, along with ground-truth regions overlaid and pictures of several agricultural fields in a subscene of the dataset (Salinas A), outlined by a red rectangle, which comprises 83x86 pixels. As shown in Fig. 7, ground truth is available for nearly two thirds of the entire scene.

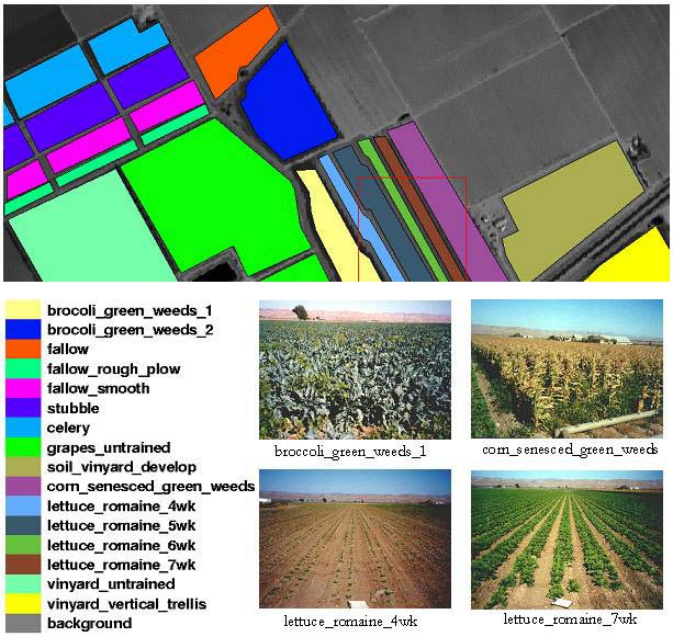

Figure 7. Salinas AVIRIS data set along with ground truth classes overlaid and pictures of several agricultural fields in a subscene called Salinas A, outlined by a red rectangle.

A random sample of 1% of the pixels was chosen from the known ground-truth of the sixteen ground-truth classes. Scale-space and scale-orientation morphological derivative profiles were extracted from the above samples. These features were used to train a neural network classifier with one hidden layer, where the number of hidden neurons was set to the square root of the product of the number of input features and information classes [24]. The trained classifier was then applied to the remaining 99% of the known ground pixels in the scene (that is, the testing data do not include any information from the

training data), yielding an average performance in the sixteen ground-truth classes of 88.21% overall accuracy when scale-space morphological features with 10 openings/closings were used (the number of closings is always equal to the number of openings). The overall accuracy was increased to 91.41%. when scale-orientation features with 10 scales and 4 orientations were used. Interestingly, an overall accuracy of 93.79% was achieved when the same scale-orientation morphological profiles were used to classify the Salinas A subscene, characterized by directional patterns. It should be noted that the entire Salinas scene is dominated by large and spectrally homogeneous regions. As a result, a very simple behavior of morphological profiles was generally observed, where each morphological feature had only one or two significant derivative maxima. Complex scenarios such as urban environments are characterized by features with several significant derivative maxima and nested regions. As a result, further experiments using real hyperspectral data collected over urban areas are highly pertinent.

B. Experiments with DAIS 7915 data comprising urban areas in Pavia, Italy

In this experiment, data from the DAIS 7915 airborne imaging spectrometer of DLR were used [24]. The data were collected at 1500 meters flight altitude over the city of Pavia, Italy, with ground resolution of 5 meters and size of 400x400 pixels (2000x2000 meters). Fig. 8(a) shows the spectral band collected at 0.639 μm by the DAIS 7915 imaging spectrometer, along with ground-truth classes superimposed. The scene is formed by a dense residential area on one side of the river, as well as open areas and meadows on the other side. Ground-truth comprises the following land-cover classes: water (blue), trees (dark green), asphalt (purple), parking lot cover (cyan), bitumen (red), brick roofs (magenta), meadows (light green), bare soil (maroon) and shadows (yellow). Following a previous research study on this scene [24], we take into account only 40 spectral bands of reflective energy, and thus skip thermal infrared bands and middle infrared bands above 1.958 μm because of low SNR in those channels.

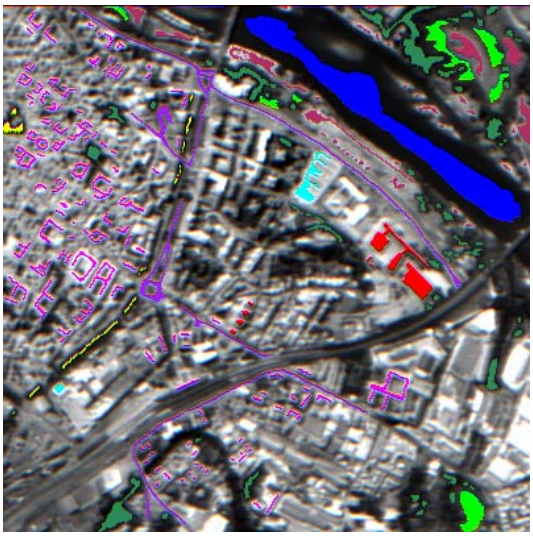

Figure 8. Spectral band at 0.639 μm of a DAIS 7915 hyperspectral image collected over the city of Pavia, Italy with overlaid ground truth classes.

A summary of the results obtained in terms of overall pure-pixel classification accuracy is given in Table 2, which shows results produced by using both scale-space and scale-orientation morphological profiles using different number of openings/closings and directional features. For the purpose of comparison, classification results produced by using original hyperspectral image pixels are also addressed. A neural network classifier with one hidden layer was trained with a random sample of 12% of the pixels from the known ground-truth of the nine ground-truth classes. The number of hidden neurons was set, based on previous work [24], according to the square root of the product of the number of input features and information classes. The trained classifier was then applied to the remaining 88% of the known ground pixels in the scene (i.e. testing data do not include any information from the training data), yielding the results shown in Table 2. In the table, directional features only apply in the case of scale-orientation profiles. As reported in Table 2, the use of both scale-space and scale-orientation morphological profiles results in higher overall accuracies than those found using original hyperspectral image pixels. In particular, 87.17% overall accuracy was achieved when scale-orientation morphological profiles with 6 scales (i.e. opening/closing operations) were applied. It can also be observed in Table 2 that, when scale-space morphological features are used, an increase in the number of opening/closing operations does not necessarily lead to improved classification accuracies, especially in complex image scenes. On other hand, the incorporation of scale-orientation morphological profiles produces classification results which are better than those found by using scale-space profiles only: 90.72% overall accuracy was achieved when morphological profiles with 6 scales and 8 orientations were used (detailed results for individual classes are reported on Table 3). The above results provide some objective confirmation of our introspection: that the incorporation of joint spatial/spectral information using scale-orientation morphological features allows very accurate modeling of real hyperspectral scenes with complex image structures.

TABLE II. OVERALL CLASSIFICATION ACCURACIES (%) PRODUCED BY A NEURAL NETWORK CLASSIFIER USING ORIGINAL IMAGE PIXELS AND EXTENDED MORPHOLOGICAL PROFILES FOR THE DAIS 7915 PAVIA SCENE

Features used for classification				
Original hyperspectral image pixels	Scale-space profiles		Scale-orientation profiles	
	6 scales	8 scales	6 scales and 4 orientations	6 scales and 8 orientations
84.16	87.17	85.64	89.97	90.72

TABLE III. CLASSIFICATION ACCURACIES (%) PRODUCED BY SCALE-ORIENTATION MORPHOLOGICAL PROFILES (6 SCALES AND 8 ORIENTATIONS) FOR THE DIFFERENT LAND-COVER CLASSES IN THE DAIS 7915 PAVIA SCENE

Class	**Color**	**Training pixels**	**Test Pixels**	**Accuracy**
Water	Blue	202	4088	99.79
Trees	Dark green	205	2219	93.73
Asphalt	Purple	203	1496	92.88
Parking lot	Cyan	201	288	89.58
Bitumen	Red	202	483	95.85
Brick roofs	Magenta	315	1923	84.14
Meadows	Light green	206	1039	80.83
Bare soil	Maroon	205	1270	86.92
Shadows	Yellow	119	122	92. 76
Overall		1858	12928	90.72

VII. Conclusions and Future Lines

In this paper, we have described new trends in processing of hyperspectral imagery by taking into account both the spatial and spectral information in simultaneous fashion. An innovative morphological endmember extraction technique for unsupervised mixed-pixel classification has been evaluated using both simulated and real data sets. Experimental results demonstrate that the combined use of spectral and spectral information can improve the results found by using the spectral information alone, in particular when a linear mixture model is used. Morphological operations are also applied to construct extended morphological profiles, which are used in this work as relevant features for supervised pure-pixel classification. Experimental results reveal that the use of scale-orientation profiles leads to higher overall classification accuracies than those found using original hyperspectral image pixels. Scale- and directional-based features can be used to complement the rich spectral information available from hyperspectral image data. A drawback of the proposed approaches is the necessity of looking at a certain range of increasing opening- and closing-by-reconstruction operations, which results in a heavy computational burden when processing high-dimensional data. In order to empower the proposed techniques with near real-time capabilities, we are currently working toward efficient implementations on massively parallel cluster computers. On other hand, although extended morphological profiles can help in creating an image feature set very effective in discrimination of complex image patterns, a lot of redundancy is evident in the resulting feature set. Therefore, feature extraction approaches such as decision boundary (DBFE) or discriminant analysis (DAFE) should be applied in the future in order to select the most important features for classification in the feature space.

Acknowledgment

The authors gratefully thank Paolo Gamba and J. Anthony Gualtieri for respectively providing DAIS 7915 and AVIRIS data sets used in pure-pixel classification examples. We also thank Jeffrey Bowles, David Gillis and Michael Winter for contributing to mixed-pixel classification experiments. Antonio Plaza gratefully acknowledges support of this research by James C. Tilton, Chein-I Chang and Robert O. Green.

References

[1] R.O. Green et al., "Imaging spectroscopy and the airborne visible/infrared imaging spectrometer (AVIRIS)," *Remote Sens. Environ.*, vol. 65, pp. 227–248, 1998.

[2] D.A. Landgrebe, *Signal theory methods in multispectral remote sensing*, John Wiley and Sons, Hoboken, New Jersey, 2003.

[3] C.-I Chang, *Hyperspectral imaging: spectral detection and classification*, Kluwer Academic Publishers, 2003.

[4] X. Jia, J.A. Richards, D.E. Ricken, *Remote Sensing digital image analysis: An introduction*. Springer, Berlin, 1999.

[5] N. Keshava, J.F. Mustard, "Spectral unmixing," *IEEE Signal Processing Magazine*, vol. 19, pp. 44-57, 2002.

[6] V. Madhok, D. Landgrebe, *Spectral-spatial analysis of remote sensing data: An image model and a procedural design*, Ph.D. dissertation, School of Elect. Eng. Comput. Sci., Purdue Univ., Lafayette, IN, 1998.

[7] D. Landgrebe, "Hyperspectral image data analysis," *IEEE Signal Processing Magazine*, vol. 19, no. 1, pp. 17-28, 2002.

[8] A. Plaza, P. Martinez, R. Perez, J. Plaza, "Spatial/spectral endmember extraction by multidimensional morphological operations," *IEEE Trans. Geosci. Remote Sensing*, vol. 40, no. 9, pp. 2025-2041, 2002.

[9] A. Plaza, "Proposal, validation and testing of a new morphological method for the analysis of hyperspectral data which combines spatial and spectral information," Ph.D. dissertation, Comput. Sci. Dept., Univ. Extremadura, Spain, 2002.

[10] P. Soille, *Morphological image analysis: Principles and applications*, 2nd Edition, Springer Verlag, Berlin, 2003.

[11] J. Serra, *Image analysis and mathematical morphology*, Academic, New York, 1982.

[12] S.R. Sternberg, "Grayscale morphology," *Comput. Vision Graphics Image Process*. vol. 35, pp. 333–355, 1986.

[13] G. Louverdis, M.I. Vardavoulia, I. Andreadis, P. Tsalides, "A new approach to morphological color processing," *Pattern Recognition,* vol. 35, pp. (2002) 1733–1741, 2002.

[14] P. Soille, M. Pesaresi, "Advances in mathematical morphology applied to geoscience and remote sensing," *IEEE Trans Geosci. Remote Sens*., vol. 40, pp. 2042–2055, 2002.

[15] M. Pesaresi and J.A. Benediktsson, "A new approach for the morphological segmentation of high-resolution satellite imagery," *IEEE Trans. Geosci. Remote Sensing*, vol.39, no.2, pp.309-320, 2001.

[16] J. Goutsias, H.J.A.M. Heijmans, K. Sivakumar, "Morphological operators for image sequences," *Computer Vision and Image Understanding*, vol. 62, pp. 326–346, 1995.

[17] J. W. Boardman, F. A. Kruse, R. O. Green, "Mapping target signatures via partial unmixing of AVIRIS data," In: *Summaries of the VI JPL Airborne Earth Science Workshop*, Pasadena, CA, 1995.

[18] M. E. Winter, "N-FINDR: An algorithm for fast autonomous spectral end-member determination in hyperspectral data," In: *Proc. SPIE Imaging Spectrometry V*, vol. 3753, pp. 266-275, 1999.

[19] J. Bowles, D. Gillis, P. Palmadesso, "New improvements in the ORASIS algorithm," in *Proc. IEEE Aerospace Conference*, Big Sky, MT, 2000.

[20] R. A. Neville, K. Staenz, T. Szeredi, J. Lefebvre, P. Hauff, "Automatic endmember extraction from hyperspectral data for mineral exploration," In: *21st Canadian Symposium Remote Sensing*, Ottawa, Canada, 1999.

[21] A. Ifarraguerri, C.-I Chang, "Multispectral and hyperspectral image analysis with convex cones," *IEEE Trans. Geosci. Remote Sensing*, vol. 37, no. 2, pp. 756-770, 1999.

[22] J. Le Moigne, J.C. Tilton, "Refining image segmentation by integration of edge and region data," *IEEE Trans. Geosci. Remote Sensing*, vol. 33, pp. 605-615, 1995.

[23] D. Heinz, C.-I Chang, "Fully constrained least squares linear mixture analysis for material quantification in hyperspectral Imagery," *IEEE Trans. Geosci. Remote Sensing*, vol. 39, pp. 529-545, 2000.

[24] J.A. Palmason, J.A. Benediktsson, K. Arnason, "Morphological transformations and feature extraction for urban data with high spectral and spatial resolution," *Proc. IEEE IGARSS*, Toulouse, France, 2003.

[25] P. Soille, H. Talbot, "Directional morphological filtering," *IEEE Trans. Patt. Anal. Machine Intell.*, vol. 23, pp. 1313-1329, 2001.

[26] A. Plaza, P. Martínez, R. Pérez, J. Plaza, "A new method for target detection in hyperspectral imagery based on extended morphological profiles," *Proc. IEEE IGARSS*, Toulouse, France, 2003.

[27] A. Plaza, P. Martínez, R. Pérez, J. Plaza, "Hyperspectral image analysis by scale-orientation morphological profiles," *Proc. SPIE Image and Signal Processing for Remote* Sensing, Barcelona, Spain, 2003.

[28] California Institute of Technology. AVIRIS (Airborne Visible/Infrared Imaging Spectrometer) homepage. Available: http://aviris.jpl.nasa.gov.

[29] M. Garcia, S. L. Ustin, "Detection of interannual vegetation responses to climatic variability using AVIRIS data in a coastal savanna in California," *IEEE Trans. Geosci. Remote Sensing*, vol. 39, no. 7, pp. 1480-1490, 2001.

[30] A. Plaza, P. Martínez, R. Pérez, J. Plaza, "A quantitative and comparative analysis of endmember extraction algorithms using hyperspectral data," *IEEE Trans. Geosci. Remote Sensing*, pending publication.